



## Mapping and spatial statistical analysis of Mars Yardangs

Jia Liu<sup>a,b</sup>, Kaichang Di<sup>a,c,d,\*</sup>, Sheng Gou<sup>a,c</sup>, Zongyu Yue<sup>a,d</sup>, Bin Liu<sup>a</sup>, Jing Xiao<sup>c</sup>, Zhaoqin Liu<sup>a</sup>

<sup>a</sup> State Key Laboratory of Remote Sensing Science, Aerospace Information Research Institute, Chinese Academy of Sciences, Beijing, China

<sup>b</sup> University of Chinese Academy of Sciences, Beijing, China

<sup>c</sup> State Key Laboratory of Lunar and Planetary Sciences, Macau University of Science and Technology, Macau, China

<sup>d</sup> CAS Center for Excellence in Comparative Planetology, Hefei, China

### ARTICLE INFO

#### Keywords:

Mars  
Yardangs  
Spatial distribution  
Length to width ratio

### ABSTRACT

Mars yardang fields were mapped using the newly available high-resolution Context Camera (CTX) mosaics (30°N to 30°S) through visual interpretation and manual digitization. We classified the Martian yardangs into three types according to their shapes: long ridge, inverted hull and curvilinear shapes, and found that the number of long ridge yardang fields account for 77.97% of all 394 yardang fields. The mapping results show that the total area of yardang fields is about 734,115 km<sup>2</sup>, within which the area of the Medusae Fossae Formation (MFF) yardangs is about 562,640 km<sup>2</sup>. We also identified and digitized individual yardang bodies wider than 500 m in the CTX mosaics. The resultant 466 yardang bodies are subsequently used as samples for statistical analysis of the morphometric parameters. Among all of the orientations, N–S is the dominant orientation of the yardang samples, and the average length and width are 5626 m and 993 m respectively. The length to width ratios vary from 1.2:1 to 46.9:1 within (30°N to 30°S) and vary from 1.5:1 to 46.9:1 in the most studied MFF. The mapping and statistical results provide important information about the spatial distribution of Mars yardangs and their morphological characteristics, which will be valuable to further study of the formation and evolution of Mars yardangs, and the aeolian environment.

### 1. Introduction

Wind action occurs on the surfaces of planetary bodies with atmosphere, such as Earth, Mars, Venus and Titan (Greeley and Iversen, 1985; Greeley et al., 1992, 1993; Silvestro et al., 2010, 2015; Ehsani, 2011). Wind-erosion geomorphology on Mars includes yardangs, ventifacts (Barlow, 2008; Bridges et al., 2014; Mangold, 2018), dark erosional streaks (Thomas et al., 1981) and scours (Bishop, 2011). Yardangs refers to elongated or streamlined hills formed by wind erosion of consolidated or semi-consolidated material (Ward, 1979, 1984; 1985; Axford et al., 1985; Melosh, 2011; Mandt and Leone, 2015). Studying of Yardangs on Mars is critical for understanding the aeolian environment and local climate, from ancient times (Ward, 1979; Barlow, 2008) to the present (Urso et al., 2018).

With the data from Mariner 9 and Viking Missions in the 1970s and 1980s, many geologists and remote sensing experts developed a strong interest in the aeolian geomorphology on Mars (e.g., Cutts and Smith, 1973; 1976; McCauley, 1973; Ward, 1979; Christensen, 1983). By image interpretation and measurement, the characteristics of Mars yardangs, such as shape, erosion direction, consistency with prevailing wind

direction, and localities, were investigated (Mutch et al., 1976, Mutch and Wolf, 1976; Ward, 1979; Scott, 1985). Research results show that yardangs are most abundant in the equatorial plains units of Mars (Ward, 1979; Greeley et al., 1993). Yardangs are relatively recent features because of very low crater densities in these units (Neukum et al., 2010). In addition, many yardang azimuths are not parallel with wind streak direction, indicating that yardangs were formed by different winds from those that formed the streaks (Ward, 1979).

In late 1990s and the 21st century, the Mars missions of United States and European Space Agency (ESA) have acquired a huge number of high-resolution images which enable more detailed study of Martian yardangs. These high-resolution images provide more accurate information of colors, shapes of yardangs, and dust accumulation and albedo change in the yardang area (Kieffer et al., 1977; Greeley, 2013; Melosh, 2011; Bridges et al., 2010). Among these studies, the Medusae Fossae Formation (MFF) has been a primary area of interest for Mars yardang research (Zimelman et al., 1997; Mandt et al., 2008; Ojha and Lewis, 2018). For example, based on Thermal Emission Imaging System (THEMIS) images and Mars Orbiter Camera (MOC) narrow-angle images, some area and volume calculations about yardangs have been made in MFF, with the

\* Corresponding author. No. 20A, Datun Road, Chaoyang District, Beijing, 100101, China.

E-mail address: [dike@radi.ac.cn](mailto:dike@radi.ac.cn) (K. Di).

<https://doi.org/10.1016/j.pss.2020.105035>

Received 6 May 2019; Received in revised form 10 June 2020; Accepted 10 June 2020

Available online 6 July 2020

0032-0633/© 2020 Elsevier Ltd. All rights reserved.

results showing that some yardangs fields covers an area of up to 40,000 km<sup>2</sup> (Mandt et al., 2008), and at least 19,000 km<sup>3</sup> of materials must have been removed (Zimelman and Griffin, 2009). Fig. 1 shows two typical examples (long ridge shape and inverted hulls shape) of yardang in the MFF in Context Camera (CTX) images.

Yardangs have been classified to different subtypes according to their shapes or sizes. For example, Mandt et al. (2008) divided the yardangs in the MFF into two subtypes: streamlined and curvilinear yardangs (Desai and Murty, 2016). Mandt and Leone (2015) classified the Martian yardangs into three subtypes by size: (1) Micro-yardang: from a few centimeters to a meter high, (2) Meso-yardang: generally, 10–15 m long and a few meters to less than a hundred meters high, (3) Mega-yardang: a wind-abraded ridge and swale features of regional extent.

Overall, most previous research on Martian yardangs mainly focuses on local region as exemplified by the MFF. However, to obtain a comprehensive understanding of the Martian yardangs, large regional and global mapping efforts with high-resolution images are necessary. Therefore, in this work we have made a large regional (30°N–30°S) mapping and spatial statistical analysis of the Martian yardangs using recently available CTX image mosaics. The mapping and analysis results can provide important information about the spatial distribution of Mars yardangs and their characteristics, which can also contribute to the study of the mechanism of the formation and evolution of Mars yardangs and aeolian environment in Martian surface (Wang et al., 2018).

## 2. Data

### 2.1. CTX mosaic

The Context Camera (CTX) is one of the imaging sensors onboard the Mars Reconnaissance Orbiter (MRO), which was launched on 12 August 2005, and entered orbit around Mars on 10 March 2006 (Zurek and Smrekar, 2007; Malin et al., 2007). The CTX images have a 6 m/pixel resolution and have covered the entire Mars. The CTX images can be downloaded from Planetary Data Systems (PDS) Geosciences Node (<http://ode.rsl.wustl.edu/mars/>) or Mars Image Explorer website (<http://themis-data.asu.edu/viewer/ctx>).

Recently, the Bruce Murray Laboratory for Planetary Visualization has produced a seam-corrected and seam-mapped mosaic of Mars rendered at 5.0 m/pixel using CTX images (Dickson et al., 2018). The CTX mosaic covers 97.3% of Mars and is subdivided into 4° × 4° and 2° × 2° tiles, which can be downloaded from (<http://murray-lab.caltech.edu/CTX/>).

The CTX mosaics are used as the base map to identify and digitize the boundaries yardang fields, and digitize the boundaries of individual

yardang bodies for necessary statistical analysis of the morphologies. Totally 5040 CTX mosaic tiles are used in this work. We have further mosaicked these tiles into 36 large mosaics in ArcGIS for more convenient use. Single CTX images are occasionally used to fill the image holes in the CTX mosaics.

### 2.2. THEMIS global image mosaic

THEMIS is an instrument onboard Mars Odyssey, which was launched on 7 April 2001 and entered Mars orbit on 24 October 2001 (Saunders et al., 2004). THEMIS provides multi-spectral thermal infrared observations in nine wavelengths at 100 m per pixel, and visible/near-infrared images in five bands at 18 m per pixel (Christensen et al., 2004). Seamless global image mosaics (Day and Night IR 100 m global mosaic at 12.57 μm) have been produced and released by the THEMIS team (Edwards et al., 2011).

Before the CTX mosaics became available, our initial mapping of Mars yardangs was done using the Day IR global mosaic, which was downloaded from the Arizona State University Mars Space Flight Facility website (<http://www.mars.asu.edu/data/>) and is used as the primary data in this research. Though the initial global interpretation and mapping of yardang fields, we found that the yardang fields (at a scale of which can be identified in THEMIS IR mosaic) mainly distribute within ±30° of the equatorial region. So in this work, we perform a regional mapping of Mars yardangs based on CTX mosaics within the region of (30°N–30°S). Using the much higher resolution CTX data, not only smaller-sized yardang fields can be identified, but also the boundaries of yardang fields can be digitized more precisely. Fig. 2 shows an example of yardang field in which the boundary of the field is blurry in the THEMIS mosaic (Fig. 2a), but it is more discernible in the CTX mosaic (Fig. 2b) and the individual yardang bodies can be delineated with high precision.

In addition to CTX and THEMIS mosaics, the Mars MGS HRSC MOLA BlendDEM Global (200 m) ([https://astrogeology.usgs.gov/search/map/Mars/Topography/HRSC\\_MOLA\\_Blend/](https://astrogeology.usgs.gov/search/map/Mars/Topography/HRSC_MOLA_Blend/)) (Ferguson et al., 2017) was used to obtain the elevation information of the yardang fields. The Mars Geologic Map (Tanaka et al., 2014; <https://pubs.usgs.gov/sim/3292/>) and USGS I-1802 A-C Mars Geologic Maps (<https://astrogeology.usgs.gov/search/map/Mars/Geology/Mars15MGeologicGISRenovation>) (Skinner et al., 2006) were used to get the geologic setting for the yardang fields.

## 3. Methods

In this research, mapping of Mars yardangs includes two levels: yardang fields and individual yardang bodies. First, yardang fields are

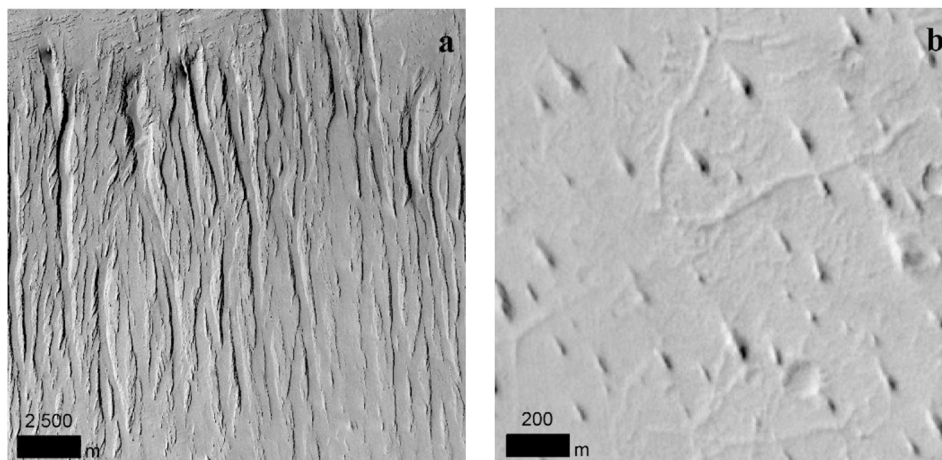


Fig. 1. Typical yardangs in the MFF. CTX image, product ID: Murray-Lab\_CTX-Mosaic\_beta01\_E152\_N00\_data, central location: (a) (152.55°E, 0.26°S), (b) (152.75°E, 2.07°N). They are long ridge shape yardangs (a) and inverted hull shape yardangs (b) according to the classification in Table 1. North is up.

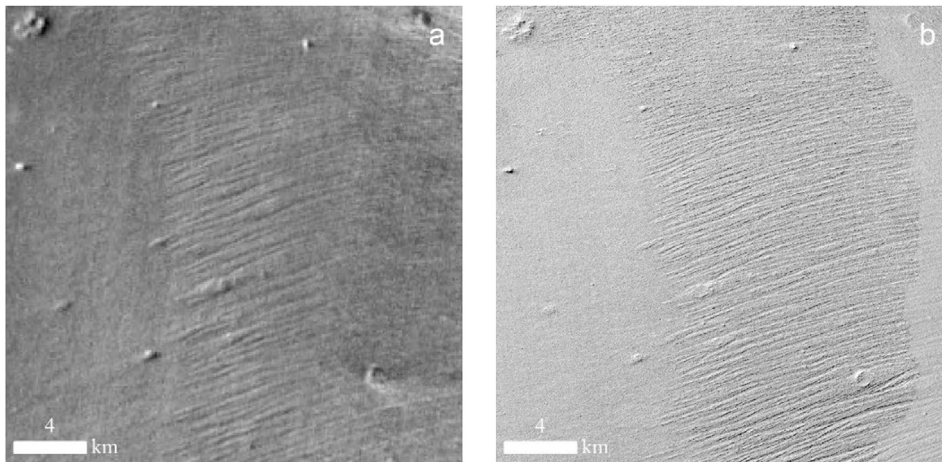


Fig. 2. A yardang field in MFF is blurry in THEMIS mosaic (a), but clearly discernable in CTX image (Image ID: Murray-Lab\_CTX-Mosaic\_beta01\_E148\_N-04\_data). North is up.

visually recognized and their boundaries are manually digitized based on the CTX mosaics in ArcGIS. Subsequently, the spatial distribution and areas of yardang fields are statistically analyzed. Second, large individual yardang bodies are identified and digitized in the CTX mosaics. The morphometric parameters of the yardang bodies are automatically calculated, and the statistics of the parameters such as average and dispersion (standard deviation) of length and width are analyzed in local areas. In order to ensure precise measurements and avoid map-projection induced distortions, map projections of Mollweide equal-area projection and Mercator projection (Snyder, 1987) are used for measuring areas and azimuths of yardang fields, respectively. It should be noted that the interpretation of yardangs and the resultant boundaries of yardang fields and individual yardang bodies are completely based on the CTX mosaics; the initial global interpretation and mapping with the THEMIS mosaic only helped to define the region of CTX mapping.

### 3.1. Classification and digitalization of yardang field boundaries

In this research, we divide Martian yardangs into three classes according to their shapes: long ridge yardang, inverted hull yardang, and curvilinear yardang. The typical images of the three yardang classes and their visual interpretation keys are as given in Table 1.

We have visually interpreted and manually digitized the boundaries of yardang fields in ArcMap based on the CTX mosaics. In our research, an area with yardangs of the same orientation and same type is defined as one yardang field. The boundaries of yardang fields are represented as polygons and are stored in a shapefile. Fig. 3 is an example of a field of MFF yardangs (central location: 151.80°E, 0.28°S). It is worth mentioning that in a large area, there may be yardangs with different wind erosion directions, or there may be different types of yardangs (see Fig. 4). In these cases, according to the definition of yardang fields, the area is split into multiple yardang fields so that each field only includes the yardangs with one orientation and one type.

### 3.2. Digitalization of individual yardang bodies and calculation of morphometric parameters

In order to study the morphometric characteristics of the Martian yardangs, we have identified, digitized the boundaries of the individual large yardang bodies (wider than 500 m) after the CTX mosaics. The basic parameters, such as length, width, azimuth (erosion direction), and area of each yardang body are calculated based on the digitized boundaries.

The definitions of length and width of long-ridge shape yardangs are illustrated in Fig. 5. Length and width definitions for inverted hull shape

yardangs are similar to that of long ridge shape yardangs. The curvilinear shape yardangs may be the initial form of the yardang development (Mandt et al., 2009; Silva et al., 2010), and the erosion tails are not distinguishable from the background terrains, making it difficult to define their lengths. Thus, the length and width of curvilinear shape yardangs are not measured.

The boundaries of yardang bodies are manually digitized as polygons in ArcGIS 10.2 platform. Then an in-house developed add-on tool of ArcGIS is used to fit an ellipse (e.g., as shown in Fig. 5) using the digitized boundary of each yardang body. Subsequently, the length, width, azimuth of a yardang can be calculated based on the fitted ellipse. Specially,

Table 1

Classification of Martian yardangs and image interpretation keys. Central locations of the key images of Long Ridge Shape, Inverted Hull Shape and Curvilinear Shape are (150.31°E, 0.8°N), (151.44°E, 1.1°N), and (179.41°W, 11.65°S), respectively.

Class	Image interpretation keys	Typical image (CTX)
<b>Long Ridge Shape</b>	The yardang has an elongated ridge with length of tens of meters to several kilometers Usually the yardang bodies in one field are parallel to each other. The wind erosion marks are obvious between the ridge and the groove.	
<b>Inverted Hull Shape</b>	The shape resembles an inverted boat hull with a blunt round or subacute bow and a tail. The length is of tens of meters to several hundred meters. Generally, the yardang bodies in one field spread regularly.	
<b>Curvilinear Shape</b>	The ridge and groove of the yardang form a circular arc shape, resembling a horseshoe or a V-shape. The yardangs extend regularly in clusters.	

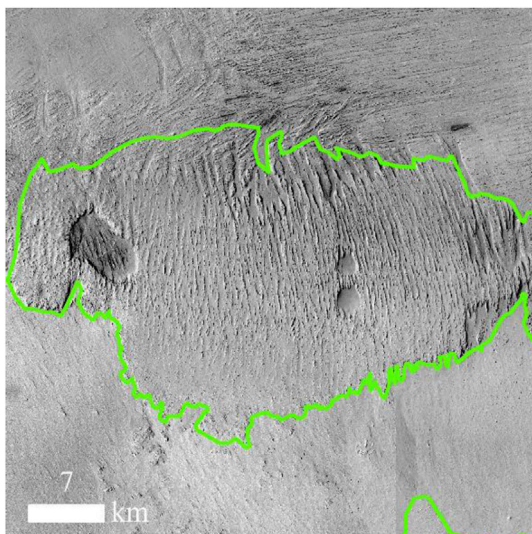


Fig. 3. A field of MFF yardangs with digitized field boundary (Image ID: Murray-Lab\_CTX-Mosaic\_beta01\_E148\_N-04\_data, central location: 152.33°W, 0.30°S). North is up.

the long axis represents the yardang length, and its orientation represents the orientation of the yardang; the short axis represents yardang width. The orientation is calculated as the azimuth of the long axis, counting clockwise from the north. Because in most cases it is very hard to determine the head and tail of a yardang body, the erosion direction can have a 180° ambiguity. Thus, the range of the azimuths is set from -90° to 90°.

Based on the parameters of the individual yardang bodies, the average length, average width, and their standard deviations are calculated for seven 30° × 30° longitude-latitude grids (Fig. 8). To draw the rose diagram in each grid, we divide the range of -90°-90° evenly into 4 bins, representing 4 azimuth directions: N-S, NW-SE, E-W and NE-SW. For better visualization, the length of each bin in the rose diagram is normalized by the maximum occurrence frequency in the grid (Fig. 8).

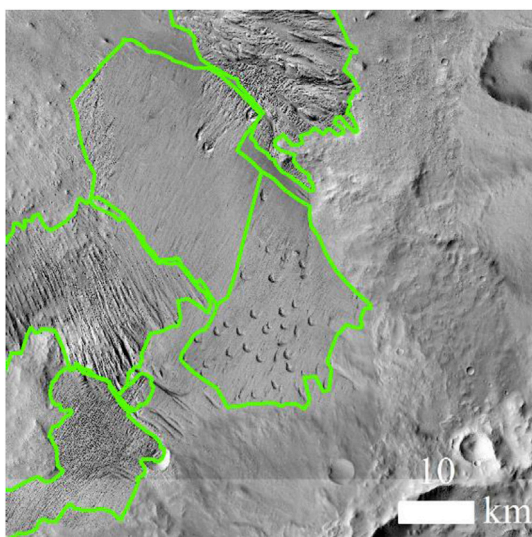


Fig. 4. An area of yardang fields with two erosion directions (NW-SE, NE-SW); and two types of yardangs (long ridge shape and curvilinear shape) (Image ID: Murray-Lab\_CTX-Mosaic\_beta01\_E-180\_N-12\_data; central location: 179.37°W, 11.52°S). North is up.

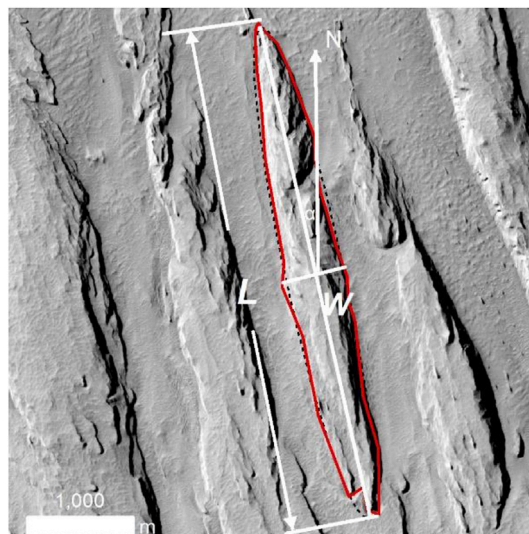


Fig. 5. Definition of length and width of long ridge shape yardangs. L is length, W is width, Red polygon is the digitized boundary of the yardang body. Length, width and orientation are calculated based on the automatically fitted ellipse (black dashed line). (Image ID: Murray-Lab\_CTX-Mosaic\_beta01\_E148\_N00\_data, central location: 150.93°E, 0.96°N) North is up.

## 4. Results

### 4.1. Spatial distribution of yardang fields

Through regional mapping within (30°N to 30°S), 394 different sized yardang fields are identified and digitized. The overall distribution of Mars yardangs is shown in Fig. 6. Total area of the yardang fields is calculated to be 734,115 km<sup>2</sup>, in which the MFF yardangs occupy an area of 562,640 km<sup>2</sup>, accounting for 86.51% of the total area. Longitudinal and latitudinal distributions of the areas of yardang fields are shown in histograms of Fig. 7. It can be observed from the top panel of Fig. 7 that the closer to the equator, the more areas of the yardang fields; and in general yardang fields within the same latitude range occupy more areas in the north than that in the south, The longitudinal distribution (bottom panel of Fig. 7) of the areas of yardang fields is quite uneven, with largest areas correspond to the MFF. In terms of elevation, 89.05% Martian yardang fields distribute in regions of negative topography, which ranges from -29 m to -4607 m.

According to the attribute table of the USGS I-1802 A-C Mars Geologic Maps (<https://astrogeology.usgs.gov/search/map/Mars/Geology/Mars15MGeologicGISRenovation>) (Skinner et al., 2006), the Martian yardangs shown in Fig. 6 mainly occur in the geotectonic units of MFF, Plateau sequence, Valles marineris interior deposits, Younger channel system material, Older channel material, Impact crater material, Tharsis montes formation, Arcadia formation, Olympus mons formation, Ridged plains material, Aeolian deposits, Older flood-plain material, Hellas assemblage, Slide material, and Smooth plains material, This geological setting information may be valuable for in-depth study of the formation and evolution of Mars yardangs.

Among the three types, long ridge yardang fields account for 77.97% of all 394 yardang fields. All of the curvilinear yardangs appear in MFF. Inverted hull yardangs often appear in the MFF and Valles marineris interior deposits according to the geotectonic unit names in the USGS geologic map (Skinner et al., 2006). The areas of long ridge, inverted hull and curvilinear yardangs account for 77.97%, 2.79%, and 4.06% of the total area, respectively.

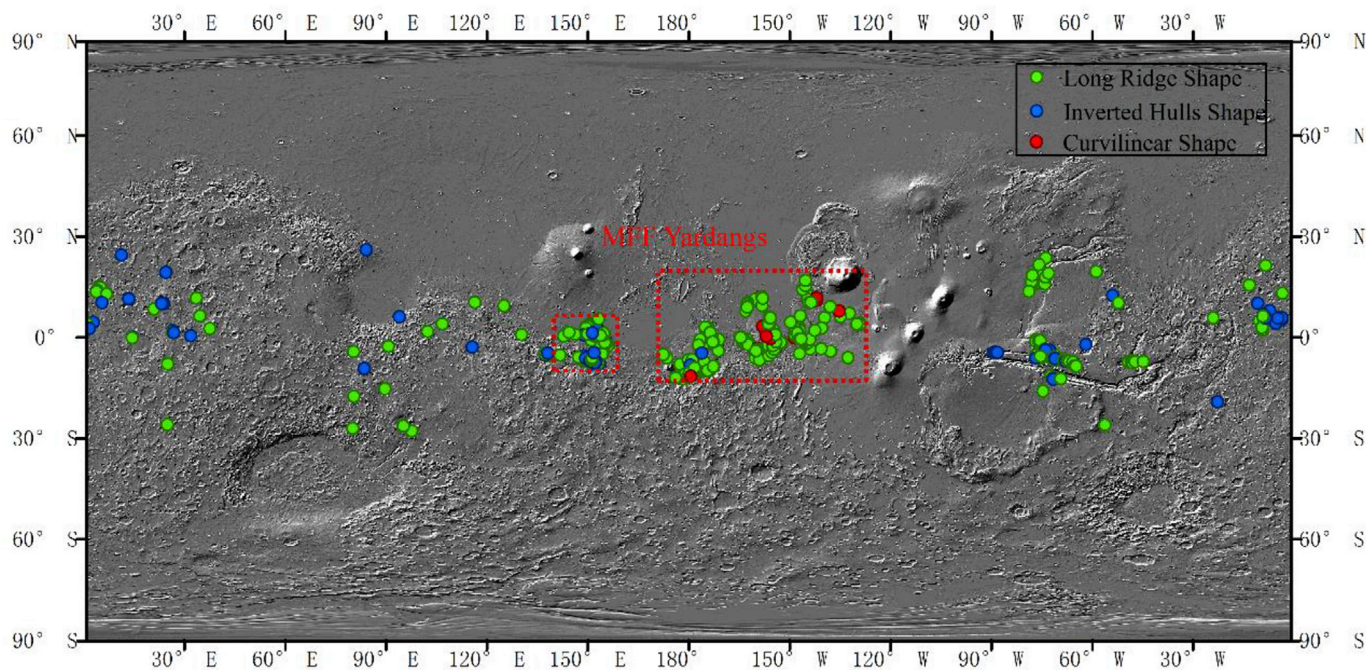


Fig. 6. Distribution of yardang fields within 30°N to 30°S. Points represent all the Martian yardangs location. Green points represent long ridge shape yardangs; blue points represent inverted hulls shape yardangs; red points represent curvilinear shape yardangs. The base map is MOLA shaded relief map.

#### 4.2. Morphometric parameters of yardang bodies

We digitized the boundaries of 882 individual yardang bodies, out of which 466 are wider than 500 m and are used as samples in the subsequent statistical analysis. It turns out that all the 466 yardangs are of long ridge shape.

The orientations of the yardangs, depicted by the azimuths of the yardang samples, are an important parameter indicating the prevailing wind directions in the process of yardang formation. The characteristics and spatial distribution of yardang orientations are shown with the rose diagram (Fig. 8), in which the map is segmented into  $30^\circ \times 30^\circ$  longitude-latitude grids. It is found that N–S is the dominant orientation and NE–SW is the secondary orientation for all the yardang samples.

Lengths of the 466 yardangs vary from 917 to 46,925 m and widths vary from 500 to 4874 m. The average length and width are 5626 m and 993 m respectively. Table 2 lists the statistics of length and width of the yardang bodies within the longitude-latitude grids in Fig. 8. Yardangs in grid 5 have both the maximum average length and the maximum deviation, and yardangs in grid 7 have both the maximum average width and the maximum deviation.

The length to width ratios of yardang samples vary from 1.2:1 to 46.9:1. As shown in the histogram (Fig. 9), the range from 1.2:1 to 10:1 is of the highest proportion, and the corresponding yardangs appear in the MFF.

Fig. 10 shows the longest yardang and the yardang with largest length to width ratio (left, THEMIS mosaic), and the widest yardang (middle, THEMIS mosaic; right, CTX mosaic). The longest yardang and the yardang with largest length to width ratio are located in Amazonian and Hesperian transition undivided unit, and the widest yardang is located in the Hesperian transition undivided unit (Tanaka et al., 2014).

## 5. Discussion

#### 5.1. Comparison with previous results

In previous research, yardang fields have been found in MFF regions (Ward, 1979, 1985; Mandt et al., 2008; Zimelman and Griffin, 2009), Aeolis quadrangle and Ares valles (Ward, 1979), Olympus Mons aureole

(Ward et al., 1985), and Tharsis Montes (Bridges et al., 2010). Mandt et al. (2008) found that MFF yardangs fields of extensive region covers an area of up to 40,000 km<sup>2</sup>, while in our results, the total area of Martian yardangs within (30°N–30°S) is 734,115 km<sup>2</sup>, and the area of the MFF yardangs is 562,640 km<sup>2</sup> based on the high-resolution CTX mosaics.

Length to width ratio, also known as aspect ratio, is one of the key morphological parameters to characterize yardangs. Ward (1979) observed that Martian yardangs has length to width ratio up to 50:1 and found that they are much larger than those known on Earth. Mandt et al. (2008) observed that the aspect ratios of MFF area megayardangs range from 3:1 to 50:1. In our results, we have analyzed 466 yardang body samples with width greater than 500 m. We found that the largest length to width ratio in the MFF is 46.9:1, which should be more reliable than previously reported.

#### 5.2. Wind regimes and yardang distribution

As shown in Fig. 6, Martian yardangs are mostly concentrated in the transitional region between northern lowland and southern highland, and enclosed by the gigantic volcanic mountains in the west and east sides. In addition, Fig. 8 shows that the dominant orientation of the yardangs is N–S. These observed spatial patterns should have a close relation with the wind regimes.

Planetary climatological studies reveal that the latitude-varying solar radiation drives significant meridional circulations in the atmosphere on Mars. The zonal-averaged meridional circulations are dominated by a huge cross-equatorial Hadley cell especially during the northern summer and winter solstice period (e.g., Mitchell et al., 2015; Xiao et al., 2019). This Hadley cell is similar to the one in the earth's atmosphere but even stronger (Mitchell et al., 2015). It is generated by the meridional ununiformed solar radiation and has been repeated over a long period. As shown by Mitchell et al. (2015, Fig. 2 therein), the near-surface winds over the equatorial region are prevailingly southerly (in summer) and northerly (in winter). Furthermore, when superimposed by the N–S slope of the transitional region and the local topography between the volcanos, the S–N winds are further strengthened.

In particular, Xiao et al. (2019) recently simulated Mars wind regime using the general circulation model MarsWRF in study of dynamical

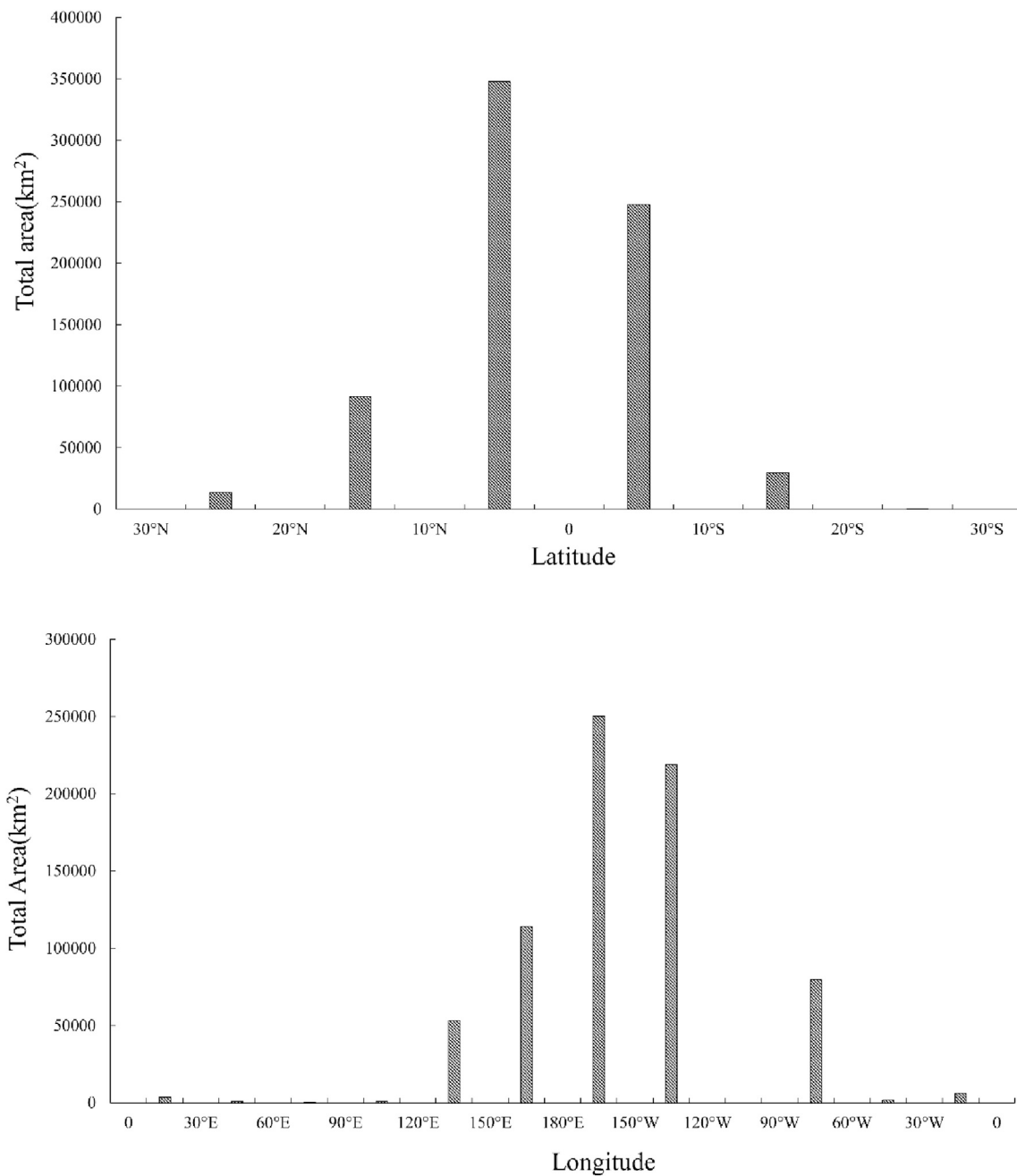


Fig. 7. Latitudinal (top panel) and longitudinal (bottom panel) distributions of yardang fields.

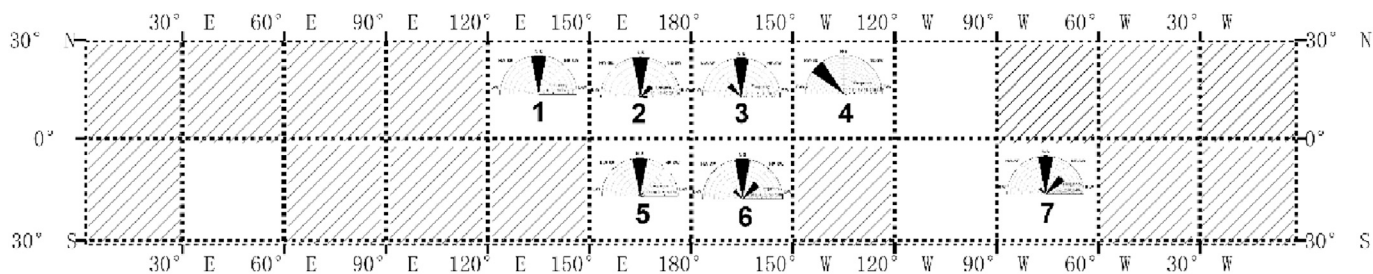


Fig. 8. Rose diagram of the orientation of Martian yardangs wider than 500 m. Yardang fields exist in the hatched grids but no yardang wider than 500 m available.

**Table 2**  
 Statistics of length and width of yardang bodies. The grid ID corresponds to that marked in Fig. 8.

Grid ID	No. of yardang bodies	Length (m)		Width (m)	
		Average	STEDV	Average	STEDV
1	40	6044.39	3480.77	691.32	224.85
2	54	4514.60	1807.80	672.36	171.24
3	20	6831.52	4301.12	772.46	164.78
4	14	5386.35	1519.37	869.13	240.99
5	96	8530.29	8427.99	714.09	243.85
6	154	4143.75	2263.77	856.36	320.74
7	88	5040.69	2063.99	930.21	416.76

processes of dust lifting. The result (Fig. 2 in Xiao et al., 2019) indicates that the wind is strongest around the equator and the wind direction is almost N-S near the surface. This is consistent with our observations of yardang distribution and dominant orientation.

**6. Conclusion**

In this research, Martian yardang fields were mapped with the newly available high-resolution CTX mosaics (30°N-30°S), and there are totally 394 yardang fields identified and characteristic parameters were also measured and analyzed. The mapping and statistical analysis results show that: (1) Yardangs on Martian surface can be categorized into three types according to their shapes, including long ridge, inverted hull and curvilinear shapes. Long ridge yardangs fields account for 77.97% of all

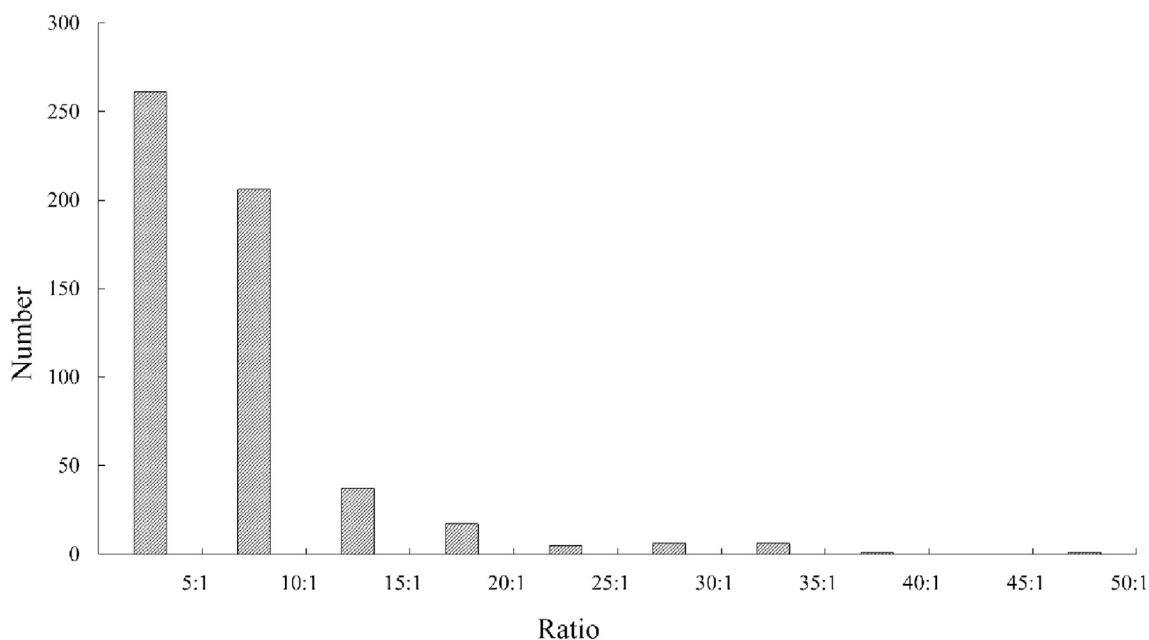


**Fig. 9.** The histogram of yardang samples length to width ratio.

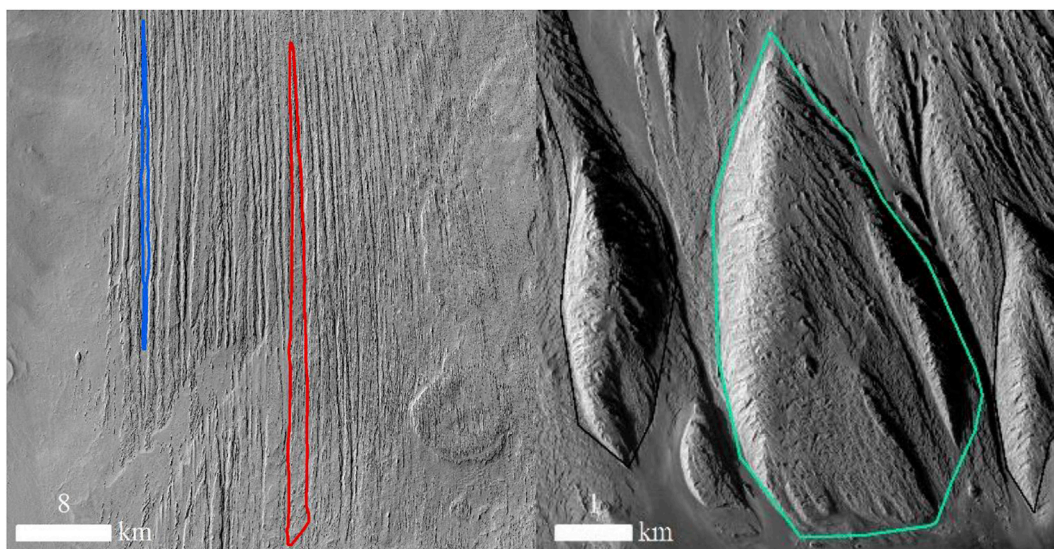


**Fig. 10.** Longest yardang (red polygon) and yardang with largest length to width ratio (blue polygon) (left, central location: 176.66°E, 10.67°S, Image ID: Murray-Lab\_CTX-Mosaic\_beta01\_E176\_N-12\_data) and widest yardang (right, central location: 71.32°W, 5.81°S, Image ID: Murray-Lab\_CTX-Mosaic\_beta01\_E068\_N04\_data). North is up.

394 yardang fields. (2) The total area of yardang fields is about 734,115 km<sup>2</sup>, within which the area of MFF yardangs is 562,640 km<sup>2</sup>. (3) The statistical analysis of 466 yardang bodies wider than 500 m indicates that the N–S is the dominant orientation. (4) The length to width ratios of long ridge shape yardangs range from 1.2:1 to 46.9:1 within (30°N–30°S) and from 1.5:1 to 46.9:1 in the most studied MFF.

The high-resolution mapping and analysis results provide comprehensive information about the spatial distribution of Mars yardangs and their characteristics. The work is significant for the study of Martian wind regimes and climate evolution. And the results can also provide important information for comparative study with the yardangs on the Earth, which is our future work.

### Declaration of competing interest

The authors declare that they have no known competing financial interests or personal relationships that could have appeared to influence the work reported in this paper.

### CRediT authorship contribution statement

**Jia Liu:** Investigation, Methodology, Visualization, Writing - original draft. **Kaichang Di:** Conceptualization, Methodology, Supervision, Writing - review & editing. **Sheng Gou:** Validation, Visualization. **Zongyu Yue:** Validation, Writing- review & editing. **Bin Liu:** Data curation. **Jing Xiao:** Formal analysis. **Zhaoqin Liu:** Software.

### Acknowledgments

The authors gratefully acknowledge the organizations, institutions and teams for making the CTX, THEMIS, MOLA, and geologic map products available. This research is supported by the Strategic Priority Research Program of Chinese Academy of Sciences (Grant No. XDB41000000), the National Natural Science Foundation of China (Grant Nos. 41771490 and 41702354), and the Science and Technology Development Fund of Macau (Grant No. 131/2017/A3). We thank Dr. Simone Silvestro and Dr. Mauro G. Spagnuolo for their insightful comments and constructive suggestions which greatly helped us to improve the manuscript.

### Appendix A. Supplementary data

Supplementary data to this article can be found online at <https://doi.org/10.1016/j.pss.2020.105035>.

### References

- Axford, W.I., Hunt, G.E., Greeley, R., 1985. Wind as a Geological Process on Earth, Mars, Venus and Titan. Cambridge university press, New York, pp. 133–144.
- Barlow, N.G., 2008. Mars: an Introduction to its Interior, Surface and Atmosphere. Cambridge university press, pp. 146–147.
- Bishop, Mark A., 2011. Aeolian scours as putative signatures of wind erosion and sediment transport direction on Mars. *Geomorphology* 125, 569–574.
- Bridges, N.T., Banks, M.E., Beyer, R.A., et al., 2010. Aeolian bedforms, yardangs, and indurated surfaces in the Tharsis Montes as seen by the HiRISE Camera: evidence for dust aggregates. *Icarus* 205 (1), 165–182.
- Bridges, N.T., Calef, F., Hallet, B., et al., 2014. The rock abrasion record at gale crater: MSL results from bradbury landing to rocknest. *J. Geophys. Res.: Planets* 119 (6), 1374–1389.
- Christensen, P.R., 1983. Eolian intracrater deposits on Mars: physical properties and global distribution. *Icarus* 56 (3), 496–518.
- Christensen, P.R., Jakosky, B.M., Kieffer, H.H., et al., 2004. The thermal emission imaging system (THEMIS) for the Mars 2001 Odyssey mission. *Space Sci. Rev.* 110, 85–130.
- Cutts, J.A., Smith, R.S.U., 1973. Eolian deposits and dunes on Mars. *J. Geophys. Res.* 78 (20), 4139–4154.
- Cutts, J.A., Blasius, K.R., Briggs, G.A., et al., 1976. North polar region of mars: imaging results from Viking 2. *Science* 194 (4271), 1329–1337.
- Desai, A., Murty, S., V., S., 2016. Morphology of yardangs within nicholson crater, mars: records of past fluvial and aeolian activities. *J. Indian Soc. Remote Sens.* 44 (6), 933–948.
- Dickson, J., Kerber, L., Fassett, C., et al., 2018. A global, blended CTX mosaic of mars with vectorized seam mapping: a new mosaicking pipeline using principles of non-

- destructive image editing. In: 49th Lunar and Planetary Science Conference 19–23 March, the Woodlands, Texas LPI Contribution No. 2083 id.2480.
- Edwards, C., Nowicki, K., Christensen, P., et al., 2011. Mosaicking of global planetary image datasets: 1. Techniques and data processing for Thermal Emission Imaging System (THEMIS) multi-spectral data. *J. Geophys. Res.* 116, E10008.
- Ehsani, A.H., 2011. Geomorphometry of Lut Mega-Yardangs. *Physical Geography Research Quarterly*. Abstract.
- Ferguson, R.L., Hare, T.M., Laura, J., 2017. HRSC and MOLA Blended Digital Elevation Model at 200m. *Astrogeology PDS Annex, U.S. Geological Survey*. [https://astrogeology.usgs.gov/search/map/Mars/Topography/HRSC\\_MOLA\\_Blend/](https://astrogeology.usgs.gov/search/map/Mars/Topography/HRSC_MOLA_Blend/).
- Greeley, R., Iversen, J.D., 1985. Wind as a Geological Process on Earth, Mars, Venus and Titan. Cambridge University Press, pp. 133–142.
- Greeley, R., Lancaster, Nicholas, Lee, Steven, Thomas, Peter, 1992. Martian Aeolian Processes, Sediments, and Features, pp. 730–766. Mars, (Chapter 22).
- Greeley, R., Skyepeck, A., Pollack, J.B., 1993. Martian aeolian features and deposits: comparisons with general circulation model results. *J. Geophys. Res. Planets* 98 (E2), 3183–3196.
- Greeley, R., 2013. Introduction to Planetary Geomorphology. Cambridge University Press, pp. 54–58.
- Kieffer, H.H., Martin, T.Z., Peterfreund, A.R., et al., 1977. Thermal and albedo mapping of mars during the Viking primary mission. *J. Geophys. Res.* 82 (28), 4249–4291.
- Malin, M.C., Bell, J.F., Cantor, B.A., et al., 2007. Context Camera investigation on board the mars reconnaissance orbiter. *J. Geophys. Res.* 112, E05S04.
- Mandt, K., Leone, G., 2015. Yardang. In: Hargitai, H., Kereszturi, A. (Eds.), *Encyclopedia of Planetary Landforms*. Springer, New York, pp. 2340–2347.
- Mandt, K.E., Silva, S.L.D., Zimbleman, J.R., Crown, D.A., 2008. Origin of the medusae Fossae Formation, mars: insights from a synoptic approach. *J. Geophys. Res.: Planets* 113, E12011.
- Mandt, K., Silva, S.D., Zimbleman, J., Wyrick, D., 2009. Distinct erosional progressions in the medusae fossae formation, mars, indicate contrasting environmental conditions. *Icarus* 204 (2), 471–477.
- Mangold, N., 2018. Surface processes. In: Rossi, A., van Gasselt, S. (Eds.), *Planetary Geology*. Springer Praxis Books. Springer, Cham, pp. 185–219.
- McCauley, J.F., 1973. Mariner 9 evidence for wind erosion in the equatorial and mid-latitude regions of Mars. *J. Geophys. Res.* 78 (20), 4123–4137.
- Mitchell, D.M., Montabone, L., Thomson, S., et al., 2015. Polar vortices on Earth and Mars: a comparative study of the climatology and variability from reanalyses. *Q. J. R. Meteorol. Soc.* 141, 550–562.
- Melosh, H.J., 2011. Planetary Surface Processes. Cambridge university press, pp. 376–377.
- Mutch, T.A., Binder, A.B., Huck, F.O., et al., 1976. The surface of Mars: there view from the Viking 1 lander. *Science* 193 (4255), 791–801.
- Mutch, T.A., Wolf, M.R., 1976. The surface of Mars: the view from the Viking 1 lander. *Science* 194 (4271), 1277–1283.
- Neukum, G., Basilevsky, A.T., Kneissl, T., et al., 2010. The geologic evolution of mars: episodicity of resurfacing events and ages from cratering analysis of image data and correlation with radiometric ages of Martian meteorites. *Earth Planet Sci. Lett.* 294 (3–4), 0–222.
- Ojha, L., Lewis, K., 2018. The density of the Medusae Fossae Formation: implications for its composition, origin, and importance in Martian history. *J. Geophys. Res.: Planets* 123.
- Saunders, R.S., Arvidson, R.E., Badhwar, G.D., et al., 2004. 2001 Mars Odyssey mission summary. *Space Sci. Rev.* 110 (1–2), 1–36.
- Scott, D.H., 1985. Global geologic mapping of mars: the western equatorial region. *Adv. Space Res.* 5 (8), 71–82.
- Skinner, J.A.J., Hare, T.M., Tanaka, K.L., 2006. Digital renovation of the atlas of mars 1: 15,000,000-scale global geologic series maps. In: Lunar & Planetary Science Conference. 37th Annual Lunar and Planetary Science Conference.
- Snyder, J.P., 1987. Map Projections: A Working Manual. USGS Professional Paper 1394. U. S. Geological Survey, Washington.
- Silva, S.L.D., Bailey, J.E., Mandt, K.E., Viramonte, J.M., 2010. Yardangs in terrestrial ignimbrites: synergistic remote and field observations on Earth with applications to Mars. *Planet. Space Sci.* 58 (4), 459–471.
- Silvestro, S., Vaz, D.A., Di Achille, G., Popa, I.C., et al., 2015. Evidence for different episodes of aeolian construction and a new type of wind streak in the 2016 ExoMars landing ellipse in Meridiani Planum, Mars. *J. Geophys. Res. Planets* 120, 760–774.
- Silvestro, S., Fenton, L.K., Vaz, D.A., et al., 2010. Ripple migration and dune activity on Mars: evidence for dynamic wind processes. *Geophys. Res. Lett.* 37, L20203.
- Tanaka, K.L., Skinner Jr., J.A., Dohm, J.M., et al., 2014. Geologic map of mars: U.S. In: *Geological Survey Scientific Investigations Map 3292 scale 1:20,000,000, pamphlet 43*. <https://pubs.usgs.gov/sim/3292/>.
- Thomas, P., Veverka, J., Lee, S., et al., 1981. Classification of wind streaks on Mars. *Icarus* 45 (1), 124–153.
- Urso, A., Matthew, Chojnacki, David, A., Vaz, 2018. Dune-yardang interactions in bequerel crater, mars. *J. Geophys. Res.: Planets* 123, 353–368.
- Wang, J., Xiao, L., Reiss, D., et al., 2018. Geological features and evolution of yardangs in the qaidam basin, Tibetan plateau (NW China): a terrestrial analogue for mars. *J. Geophys. Res.: Planets* 123 (9), 2336–2364, 5th International Planetary Dunes Workshop Special Issue.
- Ward, A.W., 1979. Yardangs on mars: evidence of recent wind erosion. *J. Geophys. Res.* 8147–8166.
- Ward, A.W., Greeley, R., 1984. Evolution of the yardangs at rogers lake, California. *Geol. Soc. Am. Bull.* 95 (7), 829.
- Ward, A.W., Doyle, K.B., Helm, P.J., et al., 1985. Global map of eolian features on Mars. *J. Geophys. Res.: Solid Earth* 2038–2056.

- Xiao, J., Chow, K.C., C. K., L., 2019. Dynamical processes of dust lifting in the northern mid-latitude region of mars during the dust storm season. *Icarus* 317, 94–103.
- Zimelman, J.R., Crown, D.A., Grant, J.A., et al., 1997. The medusae Fossae Formation, amazonis planitia, mars - evaluation of proposed hypotheses of origin. In: Lunar and Planetary Science Conference. Lunar and Planetary Science Conference, vol. 623.
- Zimelman, J.R., Griffin, L.J., 2009. HiRISE images of yardangs and sinuous ridges in the lower member of the Medusae Fossae Formation, Mars. *Icarus* 205 (1), 198–210.
- Zurek, R.W., Smrekar, S.E., 2007. An overview of the Mars Reconnaissance Orbiter (MRO) science mission. *J. Geophys. Res.* 112, E05S01.